CCFE
CULHAM CENTRE FOR FUSION ENERGY

UK Atomic Energy Authority

UKAEA-CCFE-PR(24)01

Rory Spencer, Lloyd Fletcher, Mike Gorley, Cory Hamelin, Allan Harte

Robust Assessment of Post-Localisation Hardening Behaviour in Eurofer97 using Inverse Finite Element Methods

Robust Assessment of Post-Localisation Hardening Behaviour in Eurofer97 using Inverse Finite Element Methods

Rory Spencer, Lloyd Fletcher, Mike Gorley, Cory Hamelin, Allan Harte

This is a preprint of a paper submitted for publication in Strain

Robust Assessment of Post-Localisation Hardening Behaviour in Eurofer97 using Inverse Finite Element Methods

Authors: R. Spencer, L. Fletcher, M. Gorley, C. Hamelin, A. Harte

UKAEA, Culham Science Centre, Abingdon, OX14 3DB, UK

Abstract

Constitutive behaviour of fusion-relevant steels in the post-necking regime is necessary for detailed design of future fusion device components. A Finite Element Model Updating (FEMU) procedure using Digital Image Correlation (DIC), a simulated DIC filter and novel constitutive law was developed. The effects of the DIC process and experimental noise on the uncertainty of optimised parameters were quantified using synthetic image deformation techniques. For large plasticity problems, the effect of measurement system noise was found to be negligible. The FEMU method was applied to small-scale specimens of Eurofer97 ferritic-martensitic steel of two thicknesses. Strain rate sensitivity was found to be necessary to explain observed post-UTS uniform strain due to delayed localisation onset. Local strain data from DIC measurements have been demonstrated to improve the accuracy of the identified constitutive model compared to global data alone. Additionally, DIC strain data can provide information to support the inclusion of additional model physics, such as rate sensitivity.

Keywords: Fusion, Steel, miniaturised testing, FEMU, Uncertainty, Synthetic image deformation

Introduction

Formatted: Heading 1 Char

Nuclear fusion research is moving towards detailed design for large scale demonstration reactors, intended to deliver net electricity to the grid [1], [2]. Realising commercially viable fusion necessitates a reduction in design conservatism [3]. This can be achieved by moving towards inelastic modelling and design-by analysis [4], [5]. These analyses include tests for failure modes such as: plastic collapse, ratchetting, exhaustion of ductility, fatigue and creep. Elastoplastic material models, validated over the strain range necessary for the assessment, are required. For exhaustion of ductility assessments that focus on local plastic failure, true stress-strain data is required up to the rupture strain. This will exceed the uniform strain in a standard tensile test, necessitating techniques to determine true stress-strain beyond localisation (necking). The uncertainty and credibility of design-by-analysis lifetime predictions are strongly influenced by the materials data [6]. It is therefore imperative to not only determine elastoplastic models for key fusion materials, but also quantify the uncertainty of these models. This uncertainty can then be propagated through the structural analysis to provide more robust predictions.

A key driver of fusion materials development has been to reduce the activity of materials used within fusion reactors. This has led to the production of Reduced Activation Ferritic-Martensitic (RAFM) steels, such as Eurofer97, a candidate structural steel. Its composition was engineered to reduce the activation under neutron irradiation by modifying conventional 9Cr–1Mo steel [7]. It has been subject to an extensive testing campaign aiming for code qualification within RCC-MRx, a French nuclear design code [8]. Eurofer97 exhibits strain rate sensitivity [9], [10] and after irradiation has almost no uniform elongation, spending the majority of its strain life in the post-necking region [11], [12].

The focus within the nuclear and fusion materials testing community is on reducing the size of standard mechanical tests [13]. This is driven by the size requirements for fitting specimens into materials test reactors and the subsequent challenges of handling activated material [14]. The small size of the specimens in addition to active handling considerations necessitate the use of non-contact extensometry, such as Digital Image Correlation (DIC) [15]. DIC measures full-field displacement over the entire gauge length and provides more information than extensometry.

Determining the material behaviour in miniaturised tensile specimens post-necking presents several challenges: the geometry changes, the stress state is no longer uniaxial, the strain rate is non-uniform, and ductile damage occurs. These invalidate the analytical relations between engineering and true stress-strain that apply prior to localisation. An early method to determine the true stress-strain after localisation was formulated by Bridgman [16] using the neck radius to determine a correction factor. More recent studies have proposed methods for determining the post-necking behaviour [17]. These include: analytical corrections [18], DIC and analytical relations [19], [20], DIC and local equilibrium [21], Finite Element Model Updating (FEMU) [22], [23], [24] , the Virtual Fields Method (VFM) [25] and the minimization of internal work [26].

The present work uses the FEMU approach to determine the post-necking stress-strain for the candidate fusion reactor structural steel Eurofer97. Other researchers in the fusion materials testing community have applied this technique previously, but without DIC [11], [23], [27]. This causes difficulty in optimising and validating the models. None of these studies considers strain rate sensitivity. Ductile damage using the Gurson-Tvergaard-Needleman model is considered in [27], but not the finite element mesh sensitivity this introduces.

The focus of this paper is on the development and demonstration of a robust inverse finite element method able to capture post-localisation behaviour in fusion-relevant steels. To achieve this, our study is the first to demonstrate a fast strain filter that we have developed to approximate the DIC low-pass filtering within an optimisation loop, avoiding the computational overhead of a full image deformation procedure. In addition, including strain-rate sensitivity in the identified model was found to be necessary to account for a delay in localisation after the ultimate tensile stress.

1 Inverse Identification Procedure

In this work we use a Finite Element Model Updating (FEMU) procedure to identify a plastic constitutive law including post necking behaviour. This FEMU procedure requires experimental data from the test (displacement and strain data from DIC and force), a finite element model of the test configuration, a cost function that describes the difference between the experimental data and the model, and an optimisation algorithm to minimise the cost function. The finite element model encodes the constitutive law that will be identified and at each iteration of the optimisation algorithm, the parameters of the constitutive law are updated until the difference between the experimental data and the model is minimised. In the following sections we describe each aspect of our identification procedure, starting with the finite element model.

The main drawback of the FEMU identification procedure is the computational overhead coming from the finite element model. This problem is made worse when incorporating DIC data into the cost function as direct comparison between the finite element data and the DIC data necessitates the use of appropriate uncertainty quantification so that the DIC filtering effect does not bias the identified parameters. The robust way to account for this would be to perform synthetic image deformation for each evaluation of the cost function which would further increase computational overhead. To overcome this problem, we develop a fast procedure for simulating the DIC filtering effect as described in Section 3.2.

1.1 Finite Element Model

The specimen was modelled for analysis using Abaqus/Standard (*Version 2022.HF4)* in 3D using 10,928 reduced integration linear elements (C3D8R). The mesh size in the tabs was ~0.4mm and the shoulders were refined to 0.1mm. The mesh size in the gauge section was also 0.1mm, with a region ±1mm from the centre refined by a linear decrease to the smallest size of 0.02mm. The mesh size was chosen to balance simulation accuracy and computational time. Further refinement gives negligible change in local strain at the end of the simulation. One half symmetry of the 'D-mini' specimen was modelled, shown in Figure 1, with a plane of symmetry at $z = 0$. The region between the grips was modelled to coincide with the surface visible to the DIC cameras. Displacements at the boundaries were extracted from the DIC data, linearized and applied at a

reference point. The x, y and rotational motion of this linear boundary was applied to a reference point kinematically coupled to the top surface. The bottom of the sample had a fixed displacement boundary condition to simulate a clamped condition.

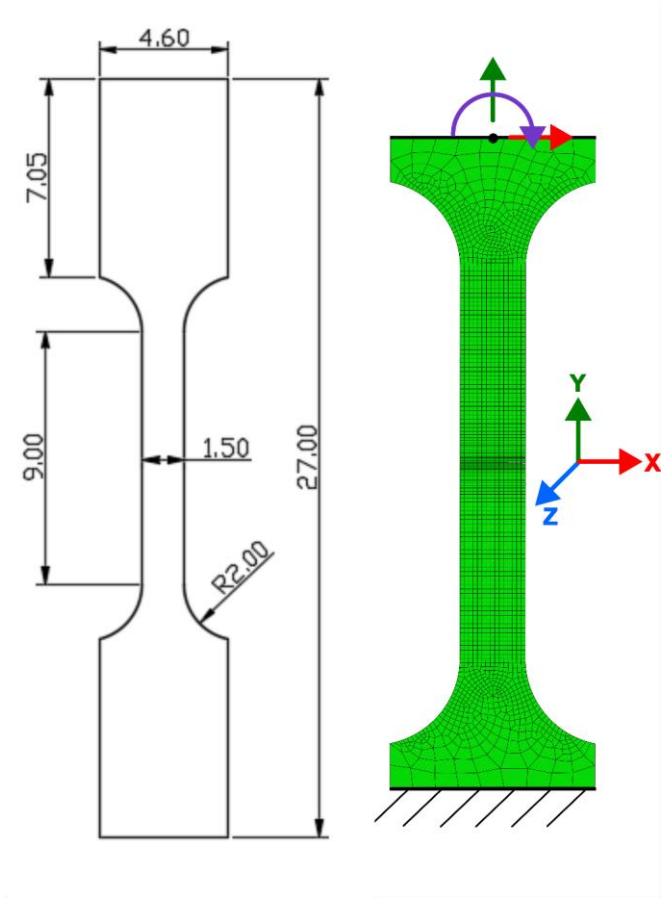

Figure 1 – Dimensions of the 'D-mini' specimen geometry in mm (left) and the Finite Element mesh used in Abaqus (right).

Reaction forces, nodal displacements and strains are output from the model at displacement steps matching those in the experiment. To reduce computation time, only steps from the ultimate tensile strength onwards are output.

1.2 Constitutive model

A suitable elastoplastic constitutive model must be chosen to ensure the model can match the expected material behaviour. In this work we require an elastoplastic law that can capture the behaviour of fusion relevant steels from yield through to necking and finally complete failure. The elastic part of the constitutive model was taken to be linear elastic and isotropic with a Young's modulus of 208 GPa and a Poisson's ratio of 0.3. For the plastic part of the constitutive law, numerous models exist to describe the post-yield, pre-necking hardening behaviour, such as the Hollomon [28], Swift [29] and Voce [30] models. These are empirical fits to data prior to necking, where analytical relationships between the engineering stress and true stress are still valid.

Beyond necking there is no guarantee that such models will provide an accurate description of the hardening behaviour [31]. Alternative models that have the flexibility to change in the post-necking region are required to better capture this behaviour.

The piecewise linear approach used in [23], [32] is advantageous when considering the effect of irradiation, which is unlikely to follow an existing hardening law. The progressive piecewise approach used by [23] can also suffer from numerical instability as identified by [32] who recommend optimising a multilinear model simultaneously. Coppieters and Kuwabara [26] used an alternative approach using a single parameter model to describe the post-necking behaviour. Pre-necking is described by the Swift model, which transitions to the single parameter model at the end of uniform elongation. Knysh and Korkolis [22] use the measured data prior to necking and describe the post necking behaviour using a cubic function.

Here we develop a modified version of the constitutive law proposed in [26]. Rather than saturating to a constant value at a strain of 1, our model saturates to a gradient. When the gradient is 0, it is equivalent to the Coppieters and Kuwabara model. We use a von Mises yield criteria with isotropic hardening. The initial behaviour prior to necking is described by a linear combination of the Swift and Voce hardening laws, chosen as the error from each model tends to cancel. i.e. the Swift model overshoots at higher strains, whereas the Voce model undershoots. Additional terms are added after necking to give the model freedom to describe the unknown behaviour. Experimental data, with an analytical conversion to true stress-strain could have been chosen to describe the pre-necking behaviour. The use of a function was preferred due to the smoothness and ease of incorporating a post-necking model. The updated yield stress is given by:

$$\sigma_{eq} = \begin{cases} a\left[K\left(\varepsilon_0 + \varepsilon_p\right)^n\right] + (1-a)\left[Y_0 + R\left(1 - e^{-k\varepsilon_p}\right)\right] & \varepsilon_p \le \varepsilon_u \\ a[K(\varepsilon_0 + \varepsilon_u)^n] + (1-a)\left[Y_0 + R\left(1 - e^{-k\varepsilon_u}\right)\right] + g(\varepsilon_p - \varepsilon_u) + Q(1 - e^{-p(\varepsilon_p - \varepsilon_u)}) & \varepsilon_p > \varepsilon_u \end{cases} \quad (1)$$

where ε_p is the equivalent plastic strain, ε_u is the equivalent plastic strain at the maximum uniform deformation, and a is the weighting factor between the Swift and Voce models in the range [0,1]. The first term is the Swift law where K is the Swift strength, ε_0 is the Swift plastic offset, and n is the Swift exponent. The second term is the Voce law where Y_0 is the Voce yield, R is the Voce saturation stress, and k is the Voce exponential term. This combination of laws was required as no single law was able to match the strain hardening behaviour between yield and UTS with sufficient accuracy.

The post-necking behaviour is described by the third and fourth terms in Eq. (1), which are only active at equivalent strains above ε_c. Two parameters control the post necking behaviour where g is the post-necking saturation gradient and p controls the sharpness of the transition to the post-necking saturation gradient. Low p values give a more gradual transition, whilst high p values give a sharper transition. The parameter Q is fixed by the choice of p, g and ε_u and the constraint of a continuous first derivative between the pre- and post- necking parts of the model. The parameter Q is given by:

$$Q = \frac{\frac{d\sigma_{eq}}{d\varepsilon_p}(\varepsilon_u) - g}{p} = \frac{aKn(\varepsilon_0 + \varepsilon_u)^{n-1} + (1-a)Rke^{-k\varepsilon_u} - g}{p}. \quad (2)$$

A series of example stress strain curves are shown in Figure 2 for the case where the parameters of the Swift and Voce laws are fixed at the values shown in Table 1 and the post-necking terms (p, g) are varied.

Table 1 – Fixed parameters for the constitutive model shown in Figure 2.

Parameter	Value	Parameter	Value
a	0.52	Y_0	582
K	919	R	159

n	0.136	k	4.4
ε_0	1.49x10^{-3}	ε_u	0.076

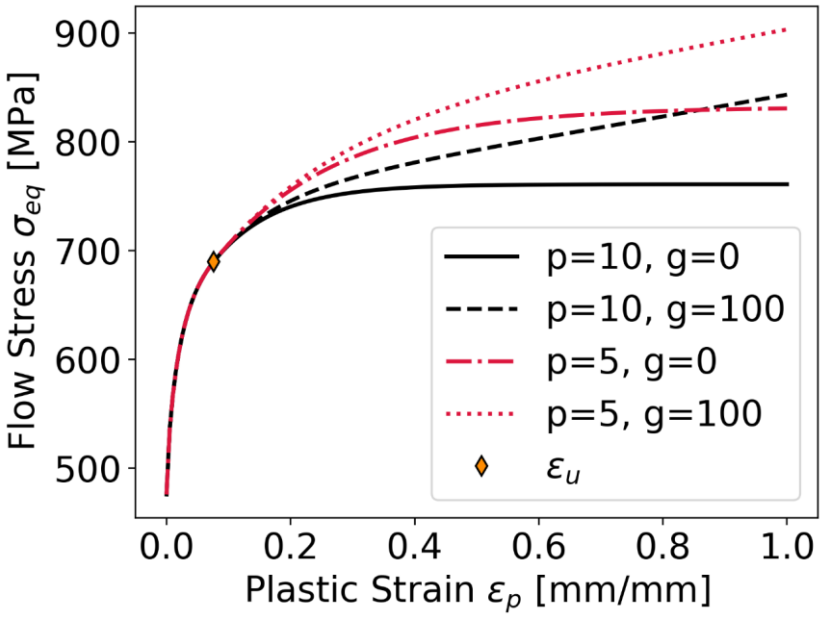

Figure 2 – Example stress-strain curves predicted using different input parameters in Eq. (1). At plastic strains lower than ε_c the model is fixed with the parameters in Table 1.

During necking the instability leads to a complex stress state in the neck which in turn leads to a non-homogenous strain rate. Ferritic martensitic steels exhibit rate sensitivity, see Section 5.3. Therefore, to account for strain effects we have used a multiplicative Johnson-Cook rate sensitivity term. The increase to the flow stress caused by Johnson-Cook rate sensitivity is given by:

$$\sigma_{rs} = \sigma_{eq}\left[1 + C\ln\frac{\dot{\varepsilon}_p}{\dot{\varepsilon}_0}\right] \tag{3}$$

where σ_{eq} is the equivalent stress from Eq. (1), $\dot{\varepsilon}_p$ is the equivalent plastic strain rate, $\dot{\varepsilon}_0$ is a reference strain rate, taken to be the nominal strain rate of the test and C controls the rate sensitivity. At strain rates less than $\dot{\varepsilon}_0$, there is no rate sensitivity. Therefore, pre-necking, C has no effect.

Here we focus on identifying the post-necking terms with our inverse identification procedure as the pre-necking Swift/Voce terms can be extracted from the uniaxial data obtained prior to necking. This leaves only 3 parameters – p, g and C – to be determined by the identification procedure.

1.3 Cost function

Here we use a two-part cost function to describe the difference between the experimental data and the finite element model. The first part of the cost function is the global component related to the force applied to the test specimen, and the second local component is related to the strain measured on the sample surface with DIC. The global component is given by the squared

difference between the force measured from the load cell in the test frame and the reaction force at the reference point in the FE model summed over all times steps, as follows:

$$L_{Global} = \frac{1}{Nu_F^2}\sum_{n=0}^{N}\left(F_n^{Exp} - F_n^{FE}\right)^2 \quad (4)$$

Where N is the total number of time steps, u_F is the noise floor for the force measurement (taken as 0.5% of the load cell range), F_n^{Exp} is the measured experimental force at the n'th step and F_n^{FE} is the reaction force from the FE model at the n'th time step.

The specimens used for this work are not tapered. Therefore, the neck can occur at any point along the gauge length. To match the strain fields in physical space it is necessary to use only a subset of the FE model surrounding the neck. In practice this means locating the origin of the (undeformed) coordinate system for both the DIC and FE data at the centre of the neck. A subset of data ±1.5mm either side of the neck can then be compared. Provided the neck does not form close the end of the gauge length, we expect this assumption to remain valid.

The local component of the cost function is the squared difference between the equivalent strain measured with DIC and the equivalent strain calculated from the FE model:

$$L_{Local} = \frac{1}{NMu_\varepsilon^2}\sum_{n=0}^{N}\sum_{m=0}^{M}\left(\varepsilon_{m,n}^{Exp} - \varepsilon_{m,n}^{FE}\right)^2 \quad (5)$$

where M is the number of data points in the region of interest, u_ε is the noise floor of the DIC strain measurement, and $\varepsilon_{m,n}^{Exp}, \varepsilon_{m,n}^{FE}$ are the equivalent strain values at point m and time n for the experiment and finite element model respectively. Note that the equivalent strain is calculated in 2D using the plane stress assumption. Beyond localisation this assumption is invalid. However, the calculation is performed for both DIC and FE strains on the visible surface. Therefore, no comparison between assumed plane stress and fully 3D equivalent strains is made.

The global force and local strain components of the cost function are then combined as follows:

$$L = \beta L_{Global} + (1-\beta)L_{Local} \quad (6)$$

where β is the weighting between the global force component and the local strain component in the range [0,1].

The force and strain components of the cost function have been normalised by their uncertainty squared, a similar approach to that used by [33]. Therefore, variations between the experiment and updated model that are less than the uncertainty, contribute less to the cost. Uncertainty on the load signal is given by the calibration certification for the load cell, in this case 0.5% of the value. For the DIC strain field a first estimate is typically given by the noise floor. However, the large deformations encountered meant that the updated reference image procedure was used. This method increases the likelihood of correlation but propagates the error. To account for this, the noise level for a given image was defined by:

$$u_{\varepsilon,n} = \sqrt{\overline{nu_{\varepsilon,1}^2}} \quad (7)$$

where $u_{\varepsilon,n}$ is the uncertainty at image n and $u_{\varepsilon,1}$ is the uncertainty at image 1, i.e. the DIC noise floor.

1.4 Optimisation Algorithm

In this work we use a Particle Swarm Optimisation (PSO) algorithm to minimise the cost function and identify the material parameters [34]. PSO is a global optimisation algorithm that does not require derivatives of the cost function. This is advantageous for identification using FEMU as the

cost function has high computational overhead and derivatives of the cost function cannot be analytically computed. The PSO algorithm also has the advantage that the cost for each particle in the swarm can be calculated in parallel allowing for ease of computational scaling. PSO has been successfully used to identify material models for hyperelasticity [35] and ductile damage [36]. The algorithm hyperparameters used in this work can be found in Appendix B.

2 Uncertainty Quantification

In this section we analyse the predicted uncertainty in the material parameters identified by our inverse identification procedure using synthetic image deformation and Monte-Carlo methods. Within this study there are numerous sources of error, shown in Figure 3. Image-based techniques such as DIC act as a low-pass filter on the underlying kinematics, leading to potential systematic errors in the identified material parameters. The magnitude of this systematic error is dependent on the number of pixels of the sensor, camera digitisation error and the selected DIC parameters (e.g., subset, step, shape function, strain window etc.). Characterising this type of systematic error is possible by simulating the imaging and subsequent DIC processing for a dataset with a known material model from a finite element model. The load cell and the DIC measurements, which both contribute to the cost function used to identify the material parameters, also include random errors coming from measurement noise (electrical noise in the relevant sensor). The effect of measurement noise on the identified parameters is captured using Monte-Carlo methods.

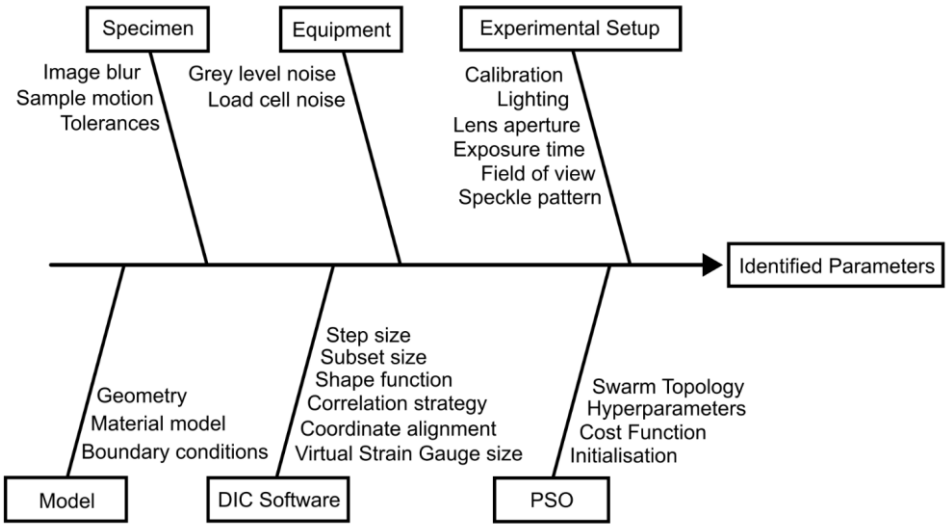

Figure 3 - Sources of error that influence DIC-identified material parameters when using synthetic image deformation with Monte Carlo methods.

2.1 Synthetic Image Deformation Method

The synthetic image deformation procedure begins with a FE model of the test. The displacement fields are then extracted and used to deform images which simulates the cameras that will be used in the experiment. These images are then processed exactly as if they are experimental data using DIC to extract the full-field kinematics before applying our inverse identification procedure. As the material parameters that are encoded in the FE model are known, they serve as reference values for uncertainty quantification. This is shown graphically in Figure 4. We generated synthetic images of our test using the MatchID Finite Element Deformation (FEDEF) module (version 2022.2.1), as

in [37]. The calibration file from the experimental DIC setup is used to generate images from the perspective of each of the cameras in the stereo setup. A ‘noise-free’ reference was created by averaging 10 static images of the specimen prior to testing.

Three synthetic datasets were created to test the optimisation process: raw FE, Synthetic Noise-Free and Synthetic Noisy, shown graphically in Figure 4. The raw FE dataset was used to verify the optimisation procedure. The Synthetic Noise-Free data allowed the analysis of any systematic errors the DIC filtering introduced, and the Noisy datasets highlighted the effect of random error on the optimisation. The initial set of deformed synthetic images are noise free and serve as a baseline for analysing systematic errors in the identification procedure. We then used Monte-Carlo sampling drawing from a Gaussian distribution with a mean of 0 and standard deviation of 2 grey levels (0.78% of the dynamic range) to generate 30 sets of noisy synthetic images representing 30 independent simulated experiments. This noise level was selected based on analysis of the static reference images taken before the experiments. The synthetic images were then run through the MatchID stereo DIC engine using the same parameters as the experiment, see Appendix A, to create our Synthetic DIC data. To create full synthetic datasets the reaction force from the FE model was coupled with the synthetic DIC data. Noise was added to the force signal by randomly sampling a uniform distribution with the magnitude of 0.5% the force value (as specified by the load-cell calibration certificate).

Table 2 – Features of the synthetically produced datasets.

Dataset	Copies	Force	Images	Processing
Raw FE	1	Noise-Free	None	None
Synthetic Noise-Free	1	Noise-Free	Noise-Free	Stereo DIC
Synthetic Noisy	30	Noisy*	Noisy**	Stereo DIC

*- Uniform distribution 0.5% force value, **-Gaussian distribution 2 grey levels.

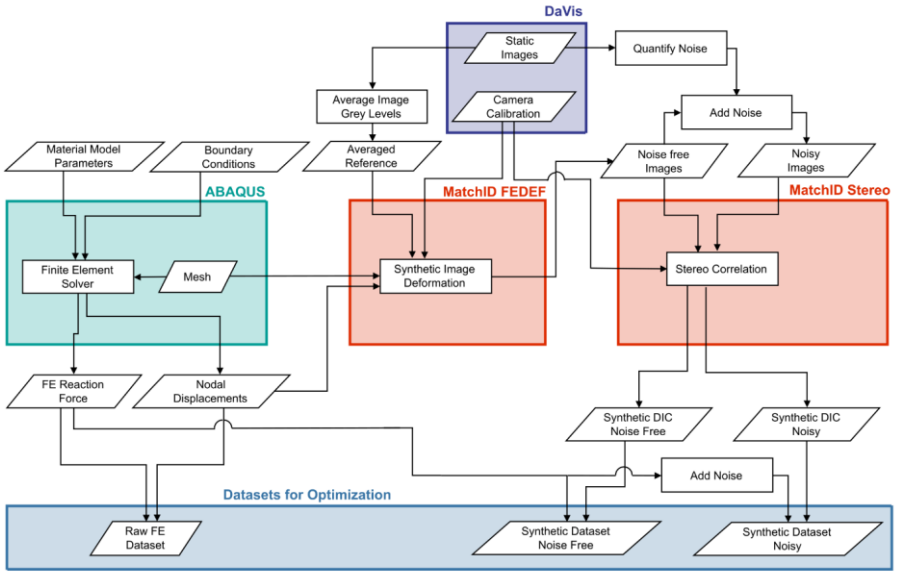

Figure 4 - Flow diagram showing the synthetic image deformation procedure described in Section 3.1 leading to the creation of 3 types of synthetic dataset.

2.2 Fast DIC Spatial Filter

DIC acts as a spatial filter, smoothing high strain gradients. This is a particular problem in the necking region. Calculating equation (5) using the raw strain values will lead to misleading results. One option to negate this problem is to employ synthetic image deformation and processing through the DIC engine as outlined in Section 3.1 in the updating process [37]. However, this is time consuming. In this work we develop a procedure that captures most of the effects of the filtering but is fast enough to be included in the updating loop. Our approach linearly interpolates the FE displacements to the DIC grid, then calculates the strain using 5x5 data point sub-windows in a similar manner to the strain calculation from displacement fields in typical DIC software. This does not account for the low pass filtering coming from the correlation algorithm itself. The improvement in matching is demonstrated in Figure 5. Subtracting the data from FE that has been run through the DIC engine from the raw FE shows significant differences, particularly in the peak strain region at the centre of the neck. The DIC levelling reduces the maximum strain value and broadens the peak. The fast filter replicates most of this effect.

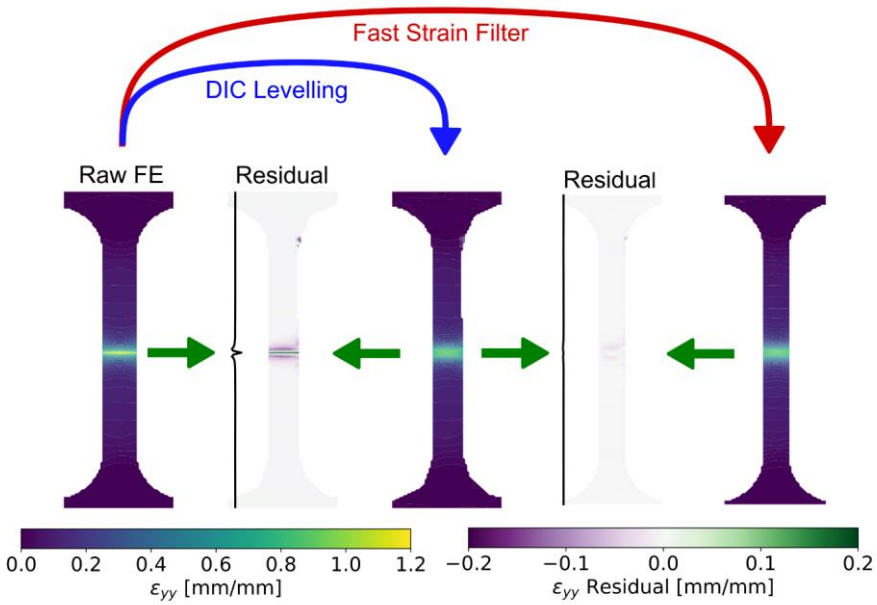

Figure 5 - Demonstrating the inclusion of a strain filter to replicate the effects of the full synthetic image deformation + DIC process.

2.3 Input FE Model

The input FE model used the parameters outlined in Table 3. Pre-necking, these are in line with the values determined from the experiment. Post necking parameters were chosen to give a strain of ~1 in the neck by the end of the test. We are therefore probing the uncertainty in a similar region of the parameter space.

For the boundary condition, a linearly ramped displacement in the y-direction was applied to the top boundary of the model, from 0 to 1.7mm in 370 steps, where 1 step is equal to 1 second. This is similar to the number of steps and time in the experiment. No rotation or x-direction translation were applied. This simplified boundary condition only applies to the Uncertainty Quantification (UQ) datasets, analysis of the experimental data uses the DIC data to generate boundary conditions.

Table 3 – Reference input parameters for verification and synthetic deformation datasets.

Parameter	Value	Parameter	Value
a	0.52	Y_0	582
K	919	R	159
n	0.136	k	4.4
ε_0	1.49×10^{-3}	ε_u	0.076
p	5	g	200
C	2.5×10^{-3}		

2.4 Verification of Identification Procedure

The raw FE dataset has been used to verify the proposed identification procedure outlined in section 2. A simplified cost function was used, as spatial interpolation and strain calculation is not required to compare FE strains to FE strains. Due to the stochastic nature of the PSO algorithm,

10 runs were performed, shown in Figure 6. The hyperparameters used are outlined in Appendix B. Due to licence limitations of the FE software the maximum number of particles that could be run simultaneously was 8. A larger number of particles would improve algorithm performance.

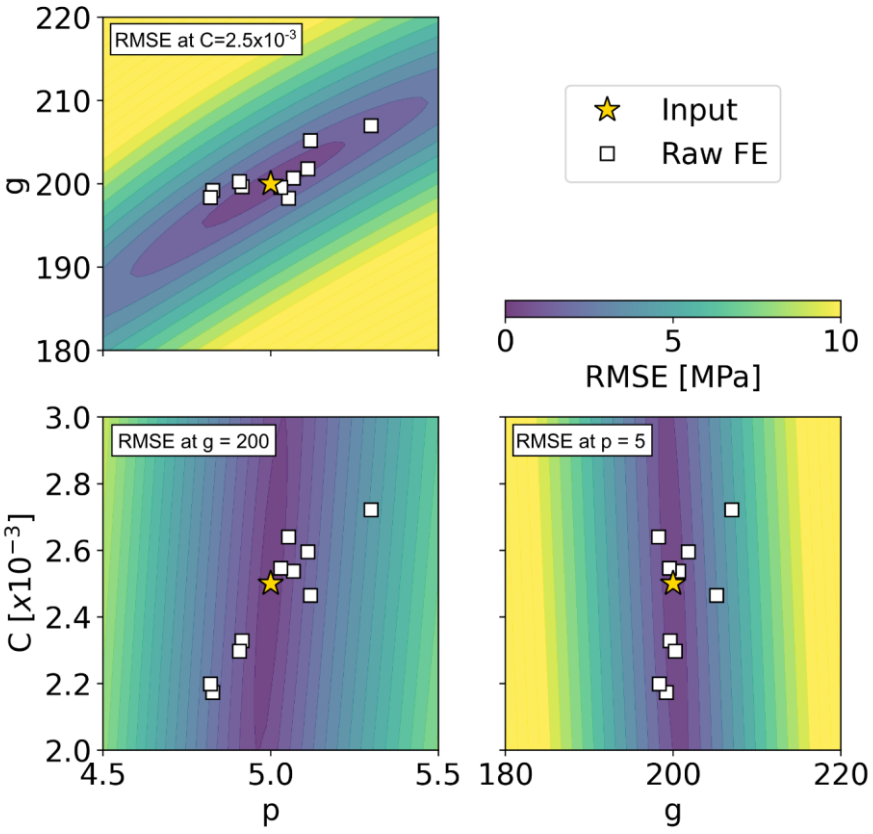

Figure 6 – Results of 10 optimisation runs, directly comparing FE strain fields. The colormap shows slices through the RMSE (Equation (8)) space at C = 2.5× 10^{-3} (top left), g = 200 (bottom left) and p = 5 (bottom right). There is clearly non-uniqueness with the model between parameters p and g over the strain and strain rate range probed in this test.

The output from the runs appears to follow a multivariate normal distribution, based on the Q-Q plot and gamma plot methods in [38], with mean and covariance below. Based on the colourmaps in Figure 6 showing the RMSE compared to the input, there is some non-uniqueness in the material model, with large changes in C giving limited impact for fixed p. This is expected as the test is not designed to probe large parts of the strain-rate parameter space, and significant changes in strain rate only occur beyond necking.

$$E[\boldsymbol{X_{FE}}] = [5.02, 201, 2.45 \times 10^{-3}]$$

$$Cov[\boldsymbol{X_{FE}}] = \begin{pmatrix} 2.2 \times 10^{-3} & 3.5 \times 10^{-1} & 2.6 \times 10^{-5} \\ 3.5 \times 10^{-1} & 8.5 & 2.8 \times 10^{-4} \\ 2.6 \times 10^{-5} & 2.8 \times 10^{-4} & 3.6 \times 10^{-8} \end{pmatrix}$$

where: $\boldsymbol{X_{FE}}$ is an array containing the converged parameters for each of the 10 runs.

The results of these optimisation runs suggest that the optimisation algorithm is working, but does highlight the effect of stochasticity in the PSO algorithm and non-uniqueness in the material model. Note that a spread in parameter space does not necessarily mean a large difference in the calculated flow curve.

2.5 Synthetic Image Deformation Results

The two synthetic datasets were used to probe different aspects of the uncertainty. The noise free dataset encodes the DIC filtering effect, all the underlying correlation choices, the calibration accuracy, the coordinate alignment, fast DIC filter, the cost function and the boundary condition extraction. All of these have the potential to introduce systematic error. The noisy dataset encodes all the above, plus the addition of random noise on the cameras and loadcell. These would be expected to increase the scatter in the optimisation results and potentially could also introduce some systematic error depending on correlation settings and cost function performance.

A series of ten optimisation runs were performed to the same synthetic noise-free dataset. A single optimisation run was performed on each of the 30 noisy datasets. The choice of thirty sets was to get sufficient data on the distribution of the converged swarms. The optimised parameter values for each run are shown in Figure 7, in addition to the raw FE verification set results.

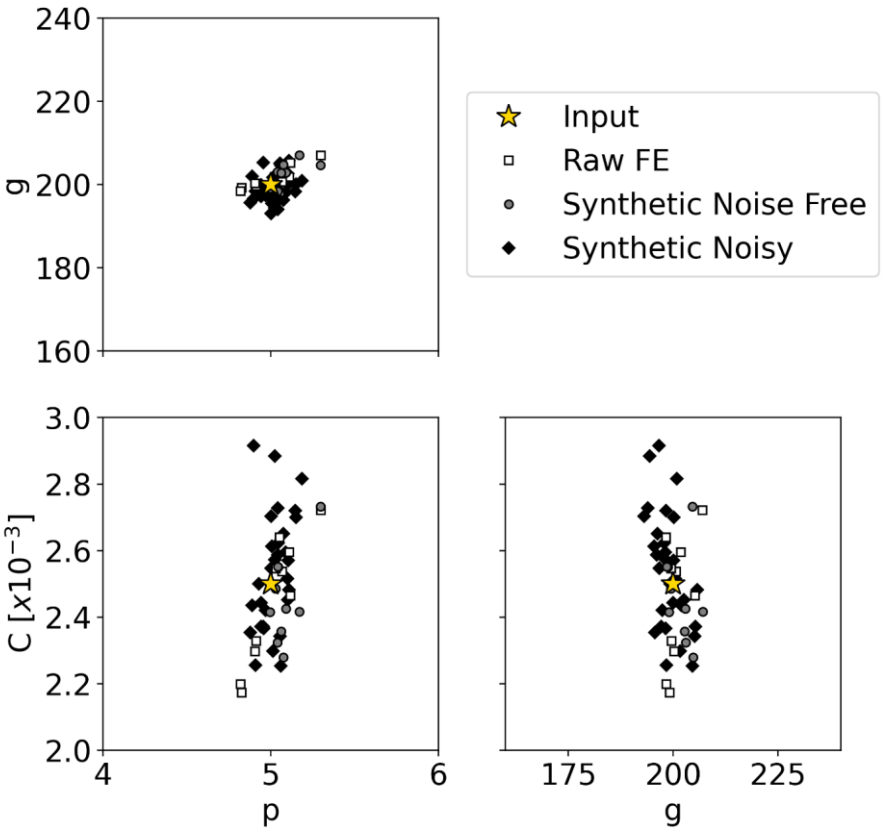

Figure 7 – Optimised parameter results for the three types of data set. Converged optimisations tend to be correlate in a similar direction to the colormaps in Figure 6.

$$E[\boldsymbol{X_{S-NF}}] = [5.04, 200, 2.48 \times 10^{-3}]$$

$$E[\boldsymbol{X_{S-N}}] = [5.02, 199, 2.54 \times 10^{-3}]$$

$$Cov[\boldsymbol{X_{S-NF}}] = \begin{pmatrix} 8.8 \times 10^{-4} & 3.0 \times 10^{-2} & 1.7 \times 10^{-7} \\ 3.0 \times 10^{-2} & 12.8 & -5.5 \times 10^{-4} \\ 1.7 \times 10^{-7} & -5.5 \times 10^{-4} & 2.7 \times 10^{-8} \end{pmatrix}$$

$$Cov[\boldsymbol{X_{S-N}}] = \begin{pmatrix} 6.8 \times 10^{-3} & 6.5 \times 10^{-1} & 5.3 \times 10^{-6} \\ 6.5 \times 10^{-1} & 11.5 & -3.1 \times 10^{-4} \\ 5.3 \times 10^{-6} & -3.1 \times 10^{-4} & 3.15 \times 10^{-8} \end{pmatrix}$$

where the parameters are ordered p, g, C, transition sharpness, saturated gradient and strain rate sensitivity respectively.

Table 4 – Summary of the synthetic data set optimisations. Best refers to the optimisation result that had the lowest value of the cost function.

Parameter	Input	Raw FE (best)	Raw FE (mean)	Syn NF (best)	Syn NF (mean)	Syn N (best)	Syn N (mean)
p	5	5.03	5.02	5.02	5.04	4.89	5.02
g	200	200	201	200	200	202	199
C [x10^{-3}]	2.5	2.55	2.45	2.49	2.48	2.44	2.54

Table 4 shows that the mean of multiple converged swarms provides a good estimate of the input parameters. Importantly, there appears to be no systematic bias introduced by the addition of the DIC filtering. The individual best run is also a good estimate, except for the case with the noisy runs. However, due to the non-uniqueness in the model, non-exact parameters do not necessarily indicate a poor fit to the model shape. Instead, the root-mean-square error (RMSE) can be used to compare the difference in the shape of the optimised and input models. The RMSE was calculated by generating a 50x50 uniform grid of values in the plastic strain-plastic strain-rate space $0.076 < \varepsilon_p > 1.42$ and $1 \times 10^{-4} > \dot{\varepsilon}_p > 1 \times 10^{-2}$. The flow stress was then calculated at each of the grid points for the input and optimised parameters using equations (1) and (3). The RMSE is then given by:

$$RMSE = \sqrt{\frac{\sum_{i=1}^{N}(x_i - \hat{x}_i)^2}{N}} \tag{8}$$

where: x_i is the input model response at point i, $\hat{x}_i$ is the optimised model response at point i and N is the number of points in the grid.

Figure 8 shows the RMSE from all runs to the raw and synthetic datasets. It can be seen that the synthetic noise-free dataset has a similar RMSE to the raw FE for all runs. The addition of noise to the dataset has led to a doubling of the RMSE, but still represents a small deviation compared to the magnitude of flow stress (~500-1000MPa). For completeness, the RMSE on the outputs from the noisy optimisation runs has been calculated, also shown in Figure 8. Despite the spread in the parameter space, the RMSE is low for all runs.

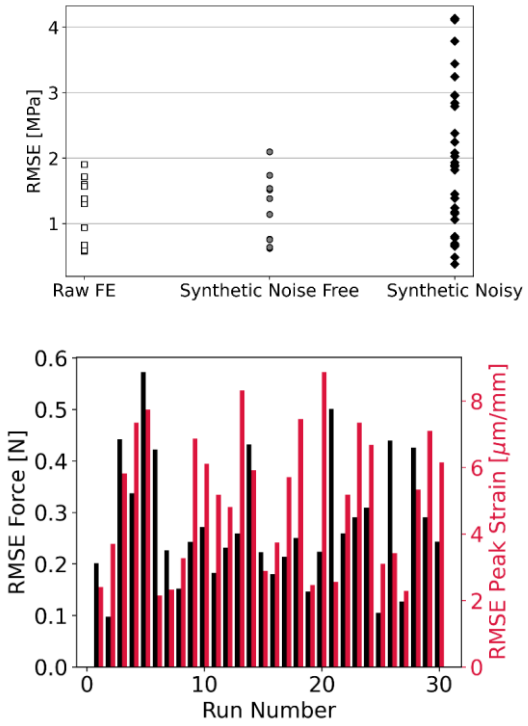

Figure 8 – RMSE on the identified model for all datasets (left) and RMSE on the output force and peak strain for the noisy optimisation runs (right).

2.6 Uncertainty Outcomes

The preceding parts of this section have demonstrated the robustness of the optimisation procedure outlined in section 2. For this specific problem and experimental setup, the introduction of the DIC spatial filtering does not introduce a systematic bias to the optimisation. Further, the random noise in the system increases the spread in the parameter space and RMSE, but also does not introduce a systematic error. This may not be the case for lower resolution or noisier cameras.

This informs some of the expected uncertainty for the optimisation to experimental data. 10 optimisation runs will be performed and the mean value of these calculated. The converged data for the noisy datasets encodes the effect of the PSO stochasticity, random error and DIC filter. Therefore, the covariance matrix calculated from these will be used as an estimate of the expected parameter spread. Note that we have explicitly not tackled the effect of model error, which will be introduced when optimising to an actual experiment.

3 Experimental Setup

3.1 Material & Specimen Geometry

The material investigated for this study was Eurofer97, a Reduced Activation Ferritic-Martensitic (RAFM) steel that is a candidate structural material for fusion reactors. Its composition was engineered to reduce the activation under neutron irradiation, by modifying conventional 9Cr–1Mo steel [7]. The specimens were Electric Discharge Machined (EDM) from the centre of a larger plate

and had the recast layer removed, giving a nominal thickness of 1mm. Two specimens were kept in this condition and two were further ground where approximately 0.125mm was removed from each side using P1200 SiC grinding paper. Surface roughness was measured on the tab sections using a Taylor Hobson Surtronic S-100.

Table 5 - Specimen conditions

Specimen	Thickness (mm)	Surface Roughness (Ra µm)	Material Removed
1	0.747	0.15	EDM recast layer + 0.125mm from each face
2	0.745	0.17	EDM recast layer + 0.125mm from each face
3	1.089	0.25	EDM recast layer only
4	1.087	0.21	EDM recast layer only

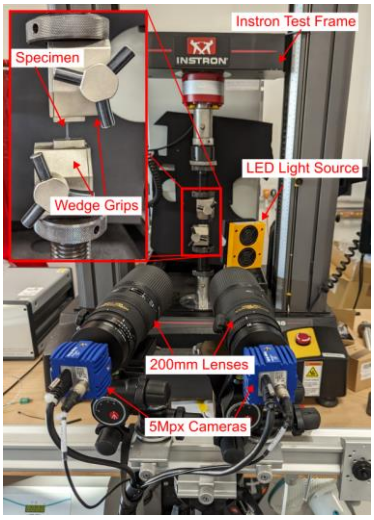

Figure 9 – Experimental testing setup for small-scale specimens.

Specimens were tested to failure using a 10kN universal test frame (*Instron 5966*) under displacement control. The specimens were clamped with wedge grips that were held in fixed position by locking collars. The crosshead was displaced at a rate of 0.54mm/min, giving a nominal strain rate of 10^{-3}/s in the specimen gauge section. Typically, small scale specimens such as these are loaded by the specimen shoulders or a using a pin through the tab ends. This gives greater control over specimen alignment and aims to prevent bending out-of-plane. However, modelling contact for these kinds of fixtures increases the complexity and computing time required for the FE simulation. Wedge grips were chosen to simplify the modelling. In addition, the location where the grip meets the specimen is within the DIC region of interest (ROI), and the displacements can be measured. These can be applied to the FE model as boundary conditions to account for any in-plane misalignment and rotation during the test.

3.2 Equipment

Displacement and strain fields on the sample were measured using a stereo DIC setup. Two 5MPx, 12bit machine vision cameras fitted with 200mm lenses, controlled by DaVis 10.2 *(LaVision)* were used to capture data. Polarising filters were fitted to both the lenses and light source to reduce unwanted reflections and increase pattern contrast. Detailed information on the setup and

processing can be found in Appendix A. Collected images were exported as .tiff files to be post-processed in the MatchID 2022.2 software suite.

4 Experimental Results & Discussion

4.1 Flow Curve Before Necking

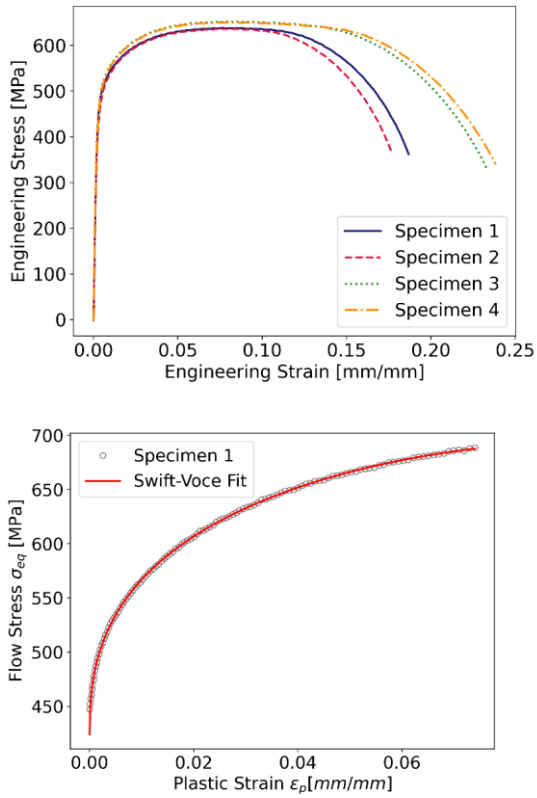

Figure 10 – Engineering stress-strain curve for all specimens (left) and example of the pre-necking flow stress vs plastic strain with fitted model described by parameters in Table 6 (right).

Engineering stress-strain curves for all specimens are shown in Figure 10, with derived engineering properties given in Table 6. All specimens have a similar yield strength, but the two thicker specimens have a greater UTS. The thicker specimens also show a greater elongation at failure, despite a similar uniform elongation.

Table 6 - Engineering properties derived from the curves shown in Figure 10.

Specimen	0.2% Offset Yield [MPa]	Ultimate Tensile Strength [MPa]	Uniform Elongation [mm/mm]*	Elongation at Failure [mm/mm]*
1	489	639	0.077	0.187
2	452	636	0.074	0.177
3	467	653	0.079	0.233
4	462	651	0.079	0.238

* Calculated using a virtual extensometer

The pre-necking terms were determined by using non-linear least squares fit to the true stress - true strain curve, calculated analytically from the average DIC strain over the gauge length up to ε_u. The equivalent plastic strain ε_u was chosen as the uniform elongation strain, i.e. the strain value at maximum force. Fitted values are shown in Table 7. The amount of uniform elongation is consistent across the specimens tested.

Table 7 – Parameters for the pre-necking region for each specimen, determined by fitting equation (1).

Specimen	a	K	n	ε_0	Y_0	R	k	ε_u
1	0.52	919	0.136	$1.49\text{x}10^{-3}$	582	159	44.0	0.076
2	0.39	992	0.169	$1.74\text{x}10^{-4}$	585	136	43.0	0.071
3	0.41	983	0.161	$3.30\text{x}10^{-4}$	605	144	40.8	0.076
4	0.50	966	0.106	$3.75\text{x}10^{-4}$	507	174	37.8	0.076

4.2 Optimisation To Experimental Data Sets

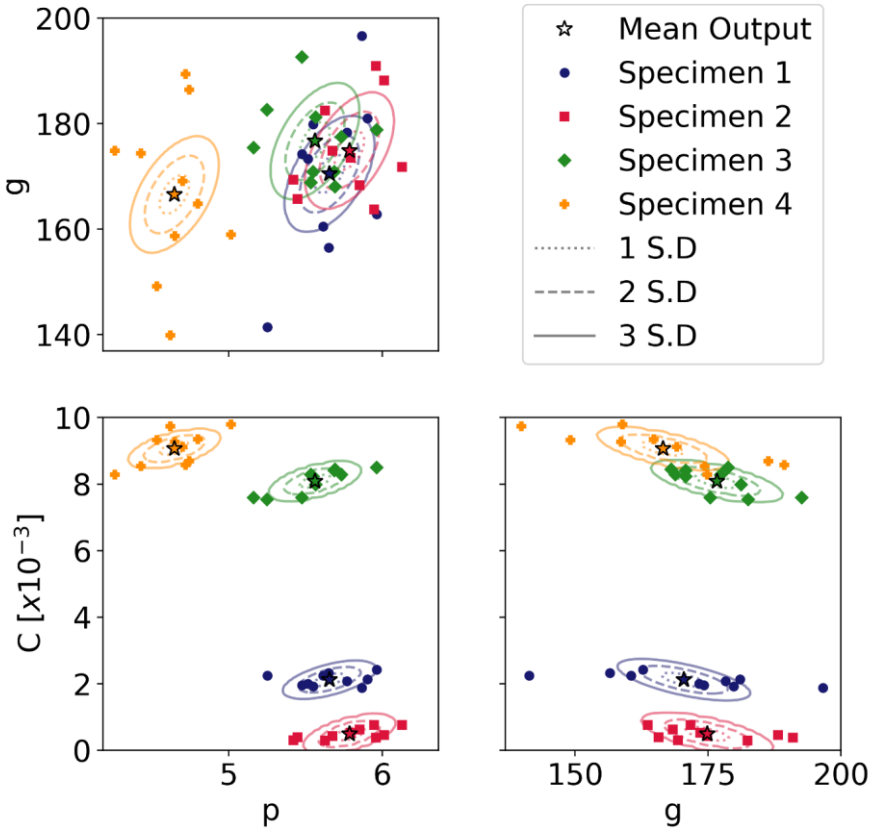

Figure 11 – Results of 10 optimisations to each experimental dataset. Contours show the number of standard deviations from the mean value, calculated using the multivariate normal in Section 3.5.

Specimen	Mean p	Mean g	Mean C
1	5.66	171	2.12×10^{-3}
2	5.79	175	4.95×10^{-4}
3	5.56	177	8.09×10^{-3}
4	4.65	167	9.07×10^{-3}

Figure 11 shows the result of 10 optimisations to each of the experimental data sets. Distances of 1, 2 and 3 standard deviations of the multivariate normal distribution derived in Section 3.5 from the mean values are shown for each specimen. Multiple points lie further than 3 standard deviations from the mean. This is likely due to error in the model form, as this was not accounted for in the uncertainty quantification of the optimisation procedure.

Specimens 1-3 are grouped well in the $p - g$ space, but specimen 4 deviates. Examination of the DIC data for specimen 4 revealed that localisation began at two separate areas on the specimen. This behaviour could not be replicated in the FE model. Further detail is provided in Appendix C.

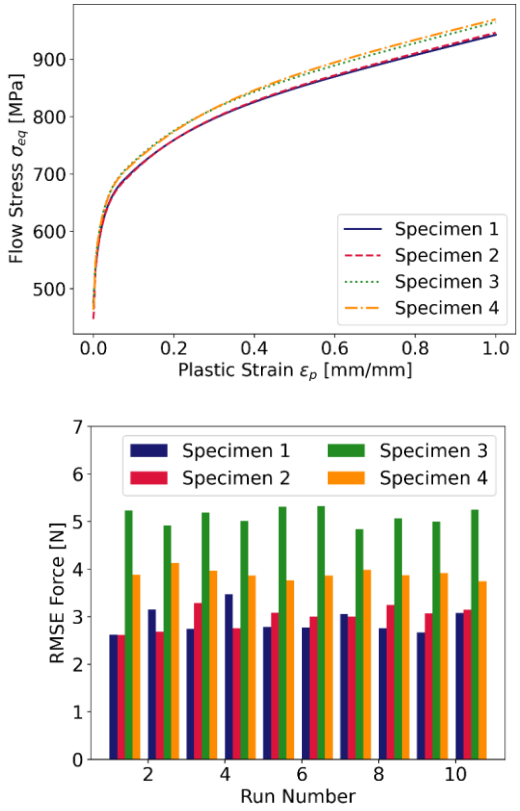

Figure 12 - RMSE on the force of the optimised models.

Figure 12 shows that despite the spread in parameter space, the derived flow curves are similar. There are two groups, corresponding to the two specimen thicknesses. The RMSE on the force suggests that the error on all runs was broadly similar for each specimen. Additionally, although the RMSE is larger than the synthetic DIC datasets, it is low compared to the magnitude of the experimental force.

The data shown in Figure 11 suggests a variation in rate sensitivity between the two thicknesses of specimens. Firm conclusions cannot be drawn due to the limited number of samples and limited sampling of strain rate space. The cause of this potential discrepancy is unclear. All specimens were subject to the same deformation rate during the test and specimen thickness was accounted for in the optimisations. Surface roughness measurements are within a factor of 2 for all specimens, suggesting it is not a surface preparation effect. There are several possible explanations: unknown physics not accounted for in the model, model form error, altered material properties due to EDM that were not fully removed in the thick specimens or the test is not rich enough to accurately determine the properties.

4.3 Effect of Rate Sensitivity

Eurofer97, as with other ferritic-martensitic steels such as T91 exhibits strain rate sensitivity [9], [10]. For the specimens tested, the strain rate in the necked region prior to failure had increased by an order of magnitude compared to the nominal strain rate for the test.

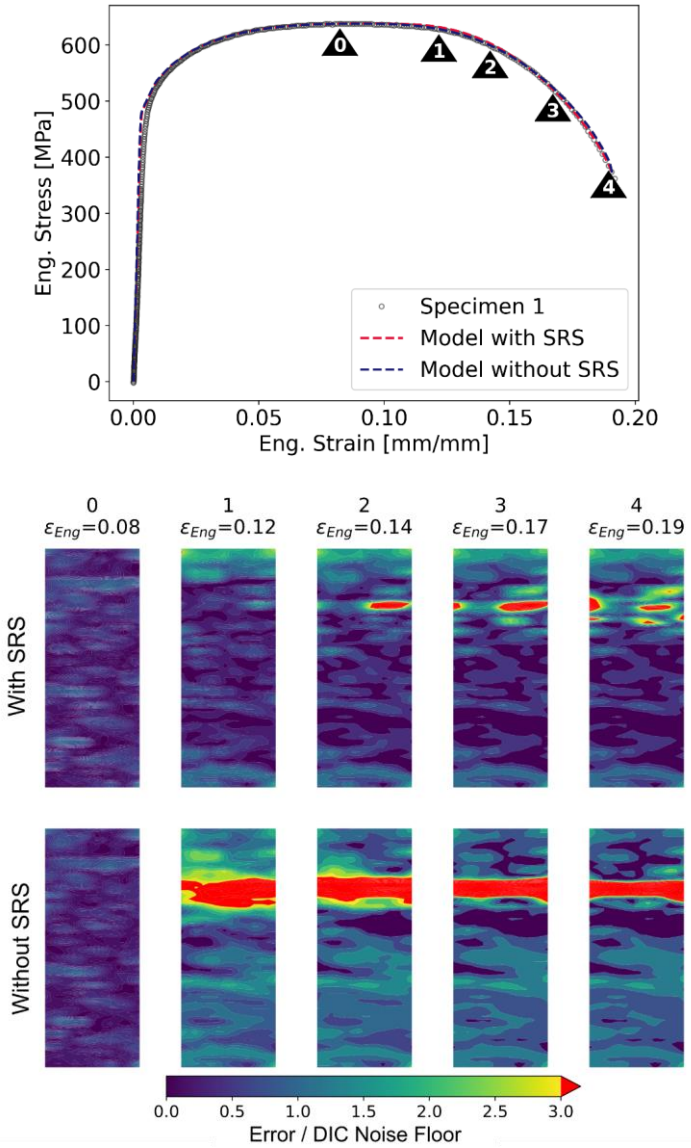

Figure 13 – Effect of the inclusion of rate sensitivity (SRS) in the material model. Engineering stress-strain curves for specimen 1 and the two different model conditions (above). Error maps of the strain field (below). Error maps were constructed by subtracting the experimental strain field from the model strain field (passed through the fast spatial filter),

then dividing by the DIC noise floor. Deviations greater than 3x the noise floor are taken to be model error. Note that the rate sensitivity improves the match between the strain behaviour.

To demonstrate the necessity of strain rate sensitivity to the optimisation result, optimisations to data from specimen 1 were performed with strain rate sensitivity and without. Results of the two runs are shown in Figure 13. These error maps were generated by subtracting the DIC axial strain field from the fast spatially filtered model strain field, then dividing by the DIC noise floor. Areas where the error exceeds 3x the noise floor are indicative of model error. The strain match is visibly worse without strain rate sensitivity at each of the shown steps. There are still regions of high error with strain rate sensitivity included, likely indicative of model-form error. For the final step the largest absolute errors were ~0.09 and ~0.17 for the models with and without SRS respectively. The DIC noise floor at this step was ~0.019, greater than the static noise-floor due to the sum of differences correlation strategy employed, see equation (7).

This also demonstrates that local strain information is vital for accurate model identification. Without the local strain data, both models appear to provide an equally good match to the global engineering stress-strain curve. Therefore, the application of FEMU with only the global data does not guarantee that the identified model is an accurate representation of local material behaviour. The inclusion of DIC data improves the likelihood of an accurate model and provides additional information to include or exclude model physics.

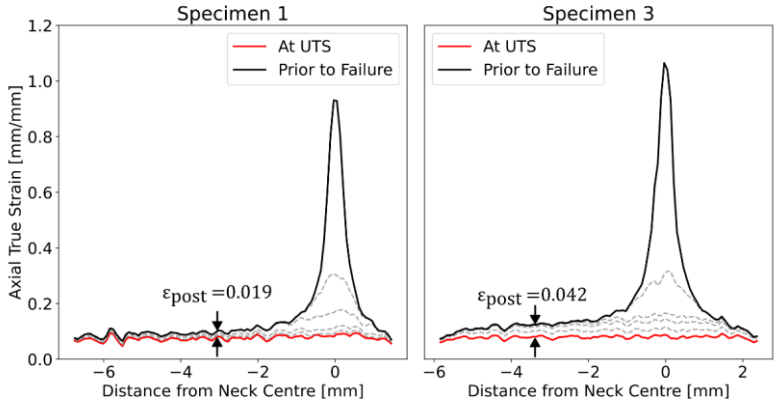

Figure 14 – Strain profiles along the vertical axis of the specimens. Both specimens show further strain beyond the uniform strain and delayed localisation. Specimen 1 (left) is 0.747mm thick, Specimen 3 (right) is 1.089mm thick..

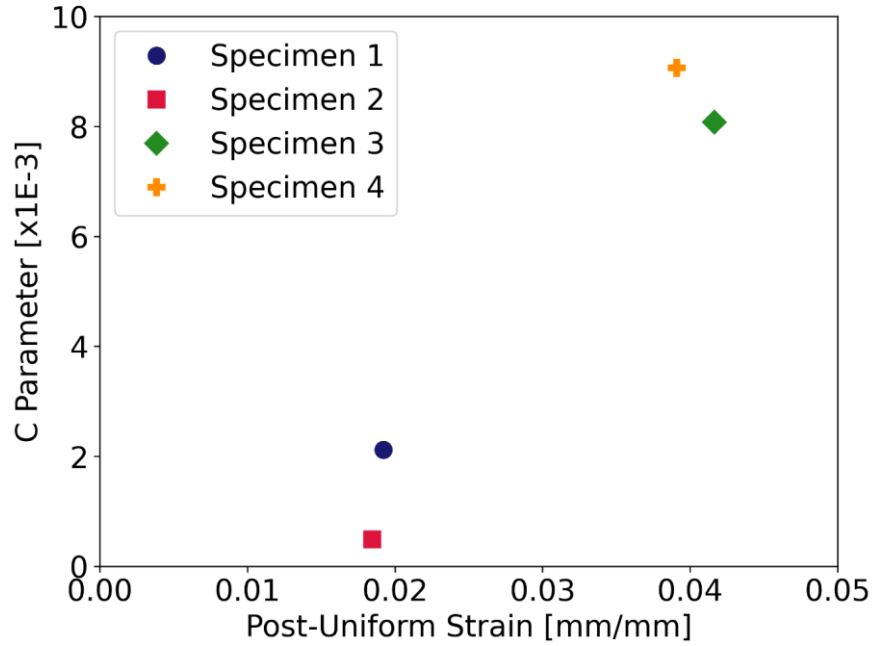
Specimen 1
Specimen 2
Specimen 3
Specimen 4
C Parameter [x1E-3]
Post-Uniform Strain [mm/mm]
0
2
4
6
8
10
0.00
0.01
0.02
0.03
0.04
0.05

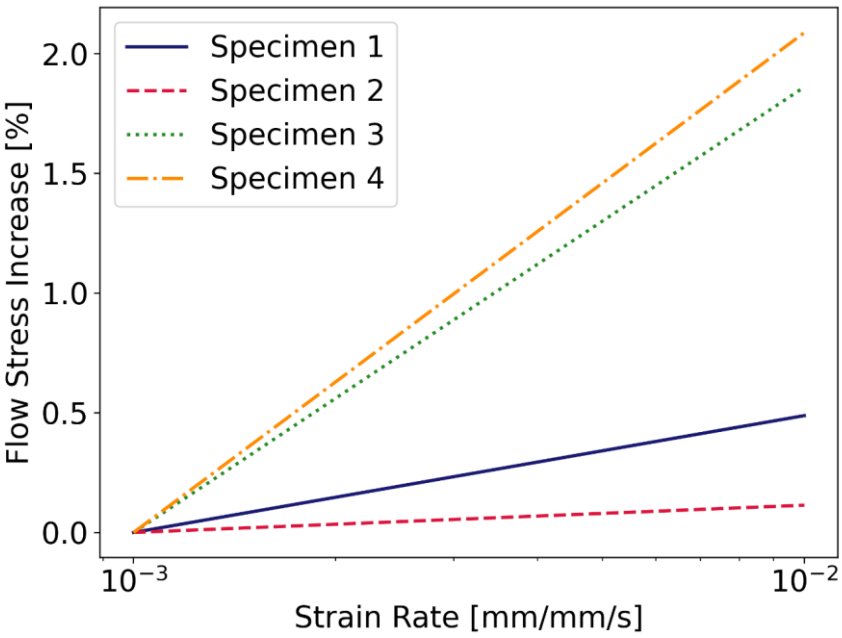
Specimen 1
Specimen 2
Specimen 3
Specimen 4
Flow Stress Increase [%]
Strain Rate [mm/mm/s]
0.0
0.5
1.0
1.5
2.0
10^{-3}
10^{-2}

Figure 15 - Relationship between post-UTS uniform strain and optimised strain rate hardening parameter C (left) and impact of the strain rate hardening parameter on the flow stress (right).

Evidence for the impact of strain rate sensitivity has been observed in the DIC data. Additional quasi-uniform deformation over the whole gauge length has been observed after the UTS, shown in Figure 14. This indicates localisation does not occur at the UTS, but after further straining. Such post-UTS uniform deformation is associated with strain rate sensitivity [39], [40], [41]. As a neck begins to form, the local cross section decreases and the strain rate increases. The increased strain rate increases the strength locally due to the rate sensitivity. This increase in strength acts to resist further decreases in the area, slowing the formation of the neck. Eventually the decrease in area wins and the neck forms. The amount of post-UTS uniform strain is related to the strain rate hardening parameter C. With the thicker specimens showing a greater post-UTS uniform strain and higher C.

Despite the different strain rate sensitivities, the impact of this on the flow stress is <2% for the strain rates encountered during this test. The primary impact on the mechanical behaviour manifests in the delay to localisation. The reason for the difference in strain rate hardening behaviour between the two specimen thicknesses is not clear. All specimens were taken from a similar volume on the original block of material. The inverse modelling approach accounts for thickness and in-plane boundary conditions. A candidate may be that the damage from the EDM process has not been completely removed from the thicker specimens, despite the reasonably similar surface roughness. Further work, with a larger sample size, is required to investigate this effect.

5 Conclusions

FEMU and DIC have been used to obtain post-necking strain and strainrate-dependent constitutive behaviour for a small-scale sample of fusion-relevant structural steel, ferritic-martensitic Eurofer97, at room temperature. Synthetic image deformation has been used to assess the error and optimisation algorithm performance. This identified that:

- For large plasticity, camera grey level and load cell noise did not introduce a systematic bias to the identified parameters, but did increase the spread in the parameter space to levels that lie within acceptable limits.
- A fast spatial filter is able to simulate DIC low pass filtering without the need to run image deformation and DIC in every optimisation loop.
- Multiple optimisation runs were required to achieve accurate results due to the stochasticity of the PSO algorithm. This leads to large computational overheads.
- More particles would lead to a better performance of the PSO algorithm, however software licence restrictions have limited the number of parallel runs used in this study. Moving towards an open-source FE solver would be advantageous.

Optimisation to the experimental data set showed:

- There is additional uncertainty that was not accounted for in the UQ, likely related to the representativeness of model form.
- Optimisation using only a global cost function can result in an inaccurate material model. Local strain information is necessary should the analyst wish to make use of post-necking stress-strain data.
- Strain-rate sensitivity is necessary in the material model to match the observed delay in localisation. The observed degree of strain rate sensitivity is linearly related to the observed post-UTS uniform strain.
- Thicker specimens showed a variation in working hardening, both pre- and post- necking. No single material model matched the behaviour of all specimens. This suggests an

unknown influence, possibly a result of machining, which is more likely to be an issue for small specimens or thin-walled structures.

6 Acknowledgements

Material used for this project was originally provided by the IAEA, as part of the Coordinated Research Project – 'Towards the Standardisation of Small Specimen Test Techniques for Fusion Applications'.

This work has been funded by the EPSRC Energy Programme, grant number EP/W006839/1. The data for this paper has been made available for public access via XXXXXX and can be accessed at https://doi.org/XXXXXXXXX.

7 References

[1] I. T. Chapman and A. W. Morris, 'UKAEA capabilities to address the challenges on the path to delivering fusion power', *Philos. Trans. R. Soc. Math. Phys. Eng. Sci.*, vol. 377, no. 2141, p. 20170436, Mar. 2019, doi: 10.1098/rsta.2017.0436.

[2] M. Gorley *et al.*, 'DEMO structural materials qualification and development', *Fusion Eng. Des.*, vol. 170, p. 112513, Sep. 2021, doi: 10.1016/j.fusengdes.2021.112513.

[3] M. Gorley, M. Fursdon, and M. Kalsey, 'Integrating Materials Engineering and Design for Fusion', *IEEE Trans. Plasma Sci.*, vol. 46, no. 5, pp. 1211–1216, May 2018, doi: 10.1109/TPS.2018.2806040.

[4] M. Fursdon, M. Li, and J. H. You, 'Enhancements in the structural integrity assessment of plasma facing components', *Fusion Eng. Des.*, vol. 146, pp. 1591–1595, Sep. 2019, doi: 10.1016/j.fusengdes.2019.02.135.

[5] M. Fursdon, J. H. You, and M. Li, 'Towards reliable design-by-analysis for divertor plasma facing components – Guidelines for inelastic assessment (part 1: Unirradiated)', *Fusion Eng. Des.*, vol. 147, Oct. 2019, doi: 10.1016/j.fusengdes.2019.06.007.

[6] J. H. You, M. Li, and K. Zhang, 'Structural lifetime assessment for the DEMO divertor targets: Design-by-analysis approach and outstanding issues', *Fusion Eng. Des.*, vol. 164, Mar. 2021, doi: 10.1016/j.fusengdes.2020.112203.

[7] A.-A. F. Tavassoli *et al.*, 'Materials design data for reduced activation martensitic steel type EUROFER', *J. Nucl. Mater.*, vol. 329–333, pp. 257–262, Aug. 2004, doi: 10.1016/j.jnucmat.2004.04.020.

[8] F. Tavassoli, 'Eurofer steel, development to full code qualification', *Procedia Eng.*, vol. 55, pp. 300–308, 2013, doi: 10.1016/j.proeng.2013.03.258.

[9] E. Cadoni, M. Dotta, D. Forni, and P. Spätig, 'Strain-rate behavior in tension of the tempered martensitic reduced activation steel Eurofer97', *J. Nucl. Mater.*, vol. 414, no. 3, pp. 360–366, Jul. 2011, doi: 10.1016/j.jnucmat.2011.05.002.

[10] M. Scapin, L. Peroni, C. Fichera, and A. Cambriani, 'Tensile Behavior of T91 Steel Over a Wide Range of Temperatures and Strain-Rate Up To 104 s−1', *J. Mater. Eng. Perform.*, vol. 23, no. 8, pp. 3007–3017, Aug. 2014, doi: 10.1007/s11665-014-1081-x.

[11] S. Knitel, P. Spätig, T. Yamamoto, H. P. Seifert, Y. Dai, and G. R. Odette, 'Evolution of the tensile properties of the tempered martensitic steel Eurofer97 after spallation irradiation at SINQ', *Nucl. Mater. Energy*, vol. 17, no. September, pp. 69–77, 2018, doi: 10.1016/j.nme.2018.09.002.

[12] E. Lucon and W. Vandermeulen, 'Overview of the tensile properties of EUROFER in the unirradiated and irradiated conditions', *J. Nucl. Mater.*, vol. 386–388, pp. 254–256, Apr. 2009, doi: 10.1016/j.jnucmat.2008.12.109.

[13] G. E. Lucas, G. R. Odette, M. Sokolov, P. Spätig, T. Yamamoto, and P. Jung, 'Recent progress in small specimen test technology', *J. Nucl. Mater.*, vol. 307–311, no. 2 SUPPL., pp. 1600–1608, 2002, doi: 10.1016/S0022-3115(02)01171-6.

[14] M. N. Gussev, R. H. Howard, K. A. Terrani, and K. G. Field, 'Sub-size tensile specimen design for in-reactor irradiation and post-irradiation testing', *Nucl. Eng. Des.*, vol. 320, pp. 298–308, Aug. 2017, doi: 10.1016/j.nucengdes.2017.06.008.

[15] T. Nozawa *et al.*, 'Non-contact strain evaluation for miniature tensile specimens of neutron-irradiated F82H by digital image correlation', *Fusion Eng. Des.*, vol. 157, no. March, p. 111663, 2020, doi: 10.1016/j.fusengdes.2020.111663.
[16] P. W. Bridgman, *Studies in Large Plastic Flow and Fracture*. New York: McGraw Hill, 1952.
[17] S. Tu, X. Ren, J. He, and Z. Zhang, 'Stress–strain curves of metallic materials and post-necking strain hardening characterization: A review', *Fatigue Fract. Eng. Mater. Struct.*, vol. 43, no. 1, pp. 3–19, Jan. 2020, doi: 10.1111/ffe.13134.
[18] S. K. Paul, S. Roy, S. Sivaprasad, and S. Tarafder, 'A Simplified Procedure to Determine Post-necking True Stress – Strain Curve from Uniaxial Tensile Test of Round Metallic Specimen Using DIC', *J. Mater. Eng. Perform.*, vol. 27, no. 9, pp. 4893–4899, 2018, doi: 10.1007/s11665-018-3566-5.
[19] S. K. Paul, S. Roy, S. Sivaprasad, H. N. Bar, and S. Tarafder, 'Identification of Post-necking Tensile Stress–Strain Behavior of Steel Sheet: An Experimental Investigation Using Digital Image Correlation Technique', *J. Mater. Eng. Perform.*, vol. 27, no. 11, pp. 5736–5743, Nov. 2018, doi: 10.1007/s11665-018-3701-3.
[20] H. Suthar, A. Bhattacharya, and S. K. Paul, 'DIC-based approach to predict post necking behavior for AA6061, AA7075 and their friction stir welded joints', *Mech. Mater.*, vol. 172, Sep. 2022, doi: 10.1016/j.mechmat.2022.104364.
[21] S. Marth, H. Å. Häggblad, M. Oldenburg, and R. Östlund, 'Post necking characterisation for sheet metal materials using full field measurement', *J. Mater. Process. Technol.*, vol. 238, pp. 315–324, 2016, doi: 10.1016/j.jmatprotec.2016.07.036.
[22] P. Knysh and Y. P. Korkolis, 'Identification of the post-necking hardening response of rate- and temperature-dependent metals', *Int. J. Solids Struct.*, vol. 115–116, pp. 149–160, Jun. 2017, doi: 10.1016/j.ijsolstr.2017.03.012.
[23] S. Knitel, P. Spätig, and H. P. Seifert, 'An inverse method based on finite element model to derive the plastic flow properties from non-standard tensile specimens of Eurofer97 steel', *Nucl. Mater. Energy*, vol. 9, pp. 311–316, Dec. 2016, doi: 10.1016/j.nme.2016.06.017.
[24] H. Zhang, S. Coppieters, C. Jiménez-Peña, and D. Debruyne, 'Inverse identification of the post-necking work hardening behaviour of thick HSS through full-field strain measurements during diffuse necking', *Mech. Mater.*, vol. 129, pp. 361–374, Jan. 2019, doi: 10.1016/j.mechmat.2018.12.014.
[25] J. H. Kim, A. Serpantié, F. Barlat, F. Pierron, and M. G. Lee, 'Characterization of the post-necking strain hardening behavior using the virtual fields method', *Int. J. Solids Struct.*, vol. 50, no. 24, pp. 3829–3842, 2013, doi: 10.1016/j.ijsolstr.2013.07.018.
[26] S. Coppieters and T. Kuwabara, 'Identification of Post-Necking Hardening Phenomena in Ductile Sheet Metal', *Exp. Mech.*, vol. 54, no. 8, pp. 1355–1371, Sep. 2014, doi: 10.1007/s11340-014-9900-4.
[27] C.-C. Chang *et al.*, 'On the equivalence of mini-flat and cylindrical tensile geometries to extract hardening law and ductility of Eurofer97', *Fusion Eng. Des.*, vol. 194, p. 113717, Sep. 2023, doi: 10.1016/j.fusengdes.2023.113717.
[28] J. Hollomon, 'Tensile Deformation', *Trans Met. Soc AIME*, vol. 162, pp. 268–90, 1945.
[29] H. W. Swift, 'Plastic instability under plane stress', *J. Mech. Phys. Solids*, vol. 1, no. 1, pp. 1–18, Oct. 1952, doi: 10.1016/0022-5096(52)90002-1.
[30] E. Voce, 'The Relationship Between Stress and Strain for Homogeneous Deformation', *J. Inst. Met.*, vol. 74, pp. 537–562, 1948.
[31] M. Dunand and D. Mohr, 'Hybrid experimental-numerical analysis of basic ductile fracture experiments for sheet metals', *Int. J. Solids Struct.*, vol. 47, no. 9, pp. 1130–1143, 2010, doi: 10.1016/j.ijsolstr.2009.12.011.
[32] K. Denys, S. Coppieters, and D. Debruyne, 'On the identification of a high-resolution multi-linear post-necking strain hardening model', *Comptes Rendus - Mec.*, vol. 346, no. 8, pp. 712–723, 2018, doi: 10.1016/j.crme.2018.06.002.
[33] F. Mathieu, H. Leclerc, F. Hild, and S. Roux, 'Estimation of Elastoplastic Parameters via Weighted FEMU and Integrated-DIC', *Exp. Mech.*, vol. 55, no. 1, pp. 105–119, Jan. 2015, doi: 10.1007/s11340-014-9888-9.
[34] M. Schwaab, E. C. Biscaia, Jr., J. L. Monteiro, and J. C. Pinto, 'Nonlinear parameter estimation through particle swarm optimization', *Chem. Eng. Sci.*, vol. 63, no. 6, pp. 1542–1552, Mar. 2008, doi: 10.1016/j.ces.2007.11.024.

[35] G. Bastos, L. Sales, N. Di Cesare, A. Tayeb, and J.-B. Le Cam, 'Inverse-Pagerank-particle swarm optimisation for inverse identification of hyperelastic models: a feasibility study', *J. Rubber Res.*, vol. 24, no. 3, pp. 447–460, Sep. 2021, doi: 10.1007/s42464-021-00113-8.
[36] J. Zhong, T. Xu, K. Guan, and B. Zou, 'Determination of Ductile Damage Parameters Using Hybrid Particle Swarm Optimization', *Exp. Mech.*, vol. 56, no. 6, pp. 945–955, 2016, doi: 10.1007/s11340-016-0141-6.
[37] P. Lava, E. M. C. Jones, L. Wittevrongel, and F. Pierron, 'Validation of finite-element models using full-field experimental data: Levelling finite-element analysis data through a digital image correlation engine', *Strain*, vol. 56, no. 4, Aug. 2020, doi: 10.1111/str.12350.
[38] F. B. Oppong and S. Y. Agbedra, 'Assessing Univariate and Multivariate Normality, A Guide For Non-Statisticians', 2016.
[39] P. P. Gillis and S. E. Jones, 'Tensile deformation of a flat sheet', *Int. J. Mech. Sci.*, vol. 21, no. 2, pp. 109–117, Jan. 1979, doi: 10.1016/0020-7403(79)90037-7.
[40] E. W. Hart, 'Theory of the tensile test', *Acta Metall.*, vol. 15, no. 2, pp. 351–355, Feb. 1967, doi: 10.1016/0001-6160(67)90211-8.
[41] A. K. Ghosh, 'The Influence of Strain Hardening and Strain-Rate Sensitivity on Sheet Metal Forming', *J. Eng. Mater. Technol.*, vol. 99, no. 3, pp. 264–274, Jul. 1977, doi: 10.1115/1.3443530.

Appendix A: DIC Setup

Table 8 -DIC Hardware Parameters

Camera	LaVision M-Lite 5M
Image Resolution	2464 x 2056 pixels
Lens	Nikon 200mm f/4D ED-IF AF Micro Nikkor
Aperture	f/8
Field-of-view	21.3 x 17.1 mm
Image Scale	122.1 px/mm
Stereo Angle	13º
Image Acquisition Rate	2Hz
Patterning Technique	Base coat of black ink, airbrushed white speckles
Pattern Feature Size (Approx)	6 px

Table 9 - DIC Analysis Parameters

DIC Software	DaVis 10.2 (Capture), MatchID 2022.2 (Processing)
Image Filtering	Gaussian
Subset Size	31
Step Size	10
Subset Shape Function	Quadratic
Matching Criterion	Zero-normalised sum of square differences (ZNSSD)
Interpolant	Local bicubic spline
Strain Window	5 px
Virtual Strain Gauge Size	71 px
Strain Formulation	Logarithmic Euler-Almansi, Q4 interpolation
Post-filtering of Strains	N/A
Displacement Noise-Floor	u: ~1 x 10^{-4}mm, v: ~1 x 10^{-4}mm, w: ~1 x 10^{-3}mm
Strain Noise-Floor	E_{xx}: ~3 x 10^{-3}, E_{yy}: ~2 x 10^{-3}, E_{xy}: ~2 x 10^{-4}

Appendix B: PSO Algorithm Settings

Table 10 – Hyperparameters of the PSO algorithm.

PSO Settings	
Topology	Local Best
Number of particles	8
Number of generations	15
w	1.2 - 0.4 linear decrease over generations
c_1	2
c_2	2
V_{max}	0.1*parameter range
β	0.2

Table 11 - Optimisation bounds for each specimen. Bounds were chosen by trial and error. If the swarm converged towards a boundary, this was modified and run again.

Specimen	p_{min}, p_{max}	g_{min}, g_{max}	C_{min}, C_{max}
1	4,6	160,240	0.002,0.003
2	4,6	130,200	0.0003,0.001
3	4,6	130,200	0.005,0.01
4	4,6	130,200	0.005,0.01

Appendix C: Specimen 4 Double Localisation

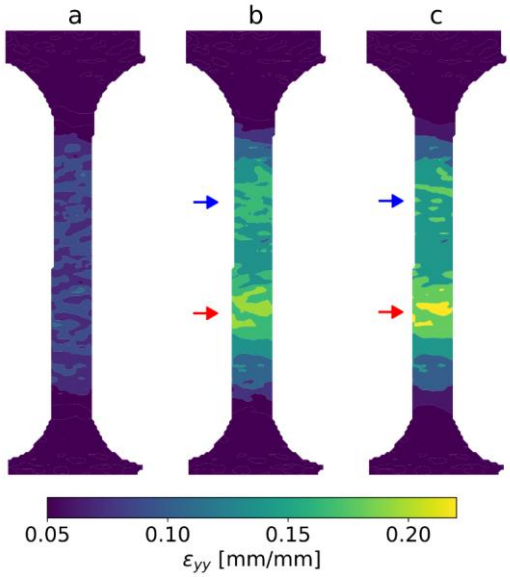

Figure 16 – Axial strain on specimen 4 (a) at the UTS 0.076 eng. strain, (b) 0.137 eng. strain and (c) 0.142 eng. strain. There appears to be localisation occurring in two locations at step b denoted by the blue and red arrows. At step c, the lower localised area (red arrow) dominates and forms the neck.

The optimisations to specimen 4 converge in a different location in the parameter space to the other three specimens. Investigation of the DIC strain maps, shown in Figure 16, suggests a possible cause. After the uniform and post-UTS uniform strain regions, localisation appears to begin at two different points on the gauge length. One region eventually dominates, forming the usual neck and leading to failure. This behaviour is not captured by the finite element model, which only localises in one region.